Remote Sensing of Environment 273 (2022) 112960

Contents lists available at ScienceDirect

Remote Sensing of Environment

journal homepage: www.elsevier.com/locate/rse

Evaluation of the tau-omega model over bare and wheat-covered flat and periodic soil surfaces at P- and L-band

Xiaoji Shen [a,*], Jeffrey P. Walker [a], Nan Ye [a], Xiaoling Wu [a], Foad Brakhasi [a], Nithyapriya Boopathi [a,b,c], Liujun Zhu [a,d], In-Young Yeo [e], Edward Kim [f], Yann Kerr [g], Thomas Jackson [h]

[a] Department of Civil Engineering, Monash University, Clayton, Australia
[b] Center of Studies in Resources Engineering, IIT Bombay, Mumbai, India
[c] IITB-Monash Research Academy, Mumbai, India
[d] Yangtze Institute for Conservation and Development, Hohai University, Nanjing, China
[e] School of Engineering, The University of Newcastle, Callaghan, Australia
[f] NASA Goddard Space Flight Center, Greenbelt, USA
[g] Centre d'Etudes Spatiales de la Biosphère, Toulouse, France
[h] USDA ARS Hydrology and Remote Sensing Laboratory (Retired), Beltsville, USA

ARTICLE INFO

Editor: Jing M. Chen

Keywords:
P-band
Passive microwave
Soil moisture retrieval
Roughness
Vegetation
Furrow

ABSTRACT

It has been over ten years since the successful launch of the first-ever dedicated satellite for global soil moisture monitoring; Soil Moisture and Ocean Salinity (SMOS). Looking towards the future, P-band (0.3–1 GHz) is a promising technique to replace or enhance the L-band (1.4 GHz) SMOS and SMAP (Soil Moisture Active Passive) missions because of an expected reduction in roughness and vegetation impact, leading to an improved soil moisture accuracy over rougher soil surfaces and more densely vegetated areas. Accordingly, this investigation evaluated the tau-omega model at P-band (0.75 GHz) using a tower-based experiment in Victoria, Australia, where brightness temperature observations were collected concurrently at P- and L-band over bare and wheat-covered flat and periodic soil surfaces. The potential to retrieve soil moisture without discriminating periodic and flat surfaces was investigated by applying the roughness and vegetation parameters calibrated for flat soil to retrieve the moisture of periodic soil. Results showed that P-band had a comparable RMSE across different roughness configurations (variations less than 0.016 m^3/m^3) for both bare and wheat-covered soil, while the L-band RMSE was only comparable for wheat-covered soil, indicating that periodic surfaces did not need to be discriminated in such scenarios. Conversely, a difference of 0.022 m^3/m^3 was observed for L-band with bare soil. A reduced vegetation impact was also demonstrated at P-band, with an RMSE of 0.029 m^3/m^3 achieved when completely ignoring the wheat existence with under 4-kg/m^2 vegetation water content, whereas at L-band the RMSE increased to 0.063 m^3/m^3. This study therefore paves the way for a successful P-band radiometer mission for obtaining more accurate global soil moisture information.

1. Introduction

The amount of water in the Earth's soil is around just 17,000 km^3 (Oki and Kanae, 2006), merely accounting for 0.05% of the total freshwater and 0.001% of the total water on/in the Earth (Shiklomanov, 1993). However, this small amount of water plays a crucial role in the Earth system because it nourishes vegetation, animals, and billions of humans. Moreover, soil moisture (SM) is a key parameter in the hydrological cycle that influences infiltration, runoff, and evapotranspiration (Seneviratne et al., 2010). Furthermore, it controls the division of the available energy at the land surface into sensible and latent heat fluxes (Koster et al., 2004).

To meet the growing need for global soil moisture data in hydrology, precision agriculture, drought, and flood forecasting, weather prediction, climate change, etc., the Soil Moisture and Ocean Salinity (SMOS) satellite (Kerr et al., 2010) and the Soil Moisture Active Passive (SMAP) satellite (Entekhabi et al., 2010) were launched in 2009 and 2015, respectively. Both use L-band (1.4 GHz/21-cm wavelength) radiometers

* Corresponding author.
E-mail address: xiaoji.shen@monash.edu (X. Shen).

https://doi.org/10.1016/j.rse.2022.112960
Received 22 September 2021; Received in revised form 12 February 2022; Accepted 15 February 2022
Available online 5 March 2022

to measure the microwave emission from the Earth in the form of brightness temperature (TB), which is a function of the emissivity and physical temperature of the target. The emissivity of bare soil varies from approximately 0.5 for smooth and very wet soil to close to 1 for rough and very dry soil (Ulaby et al., 1982), being the primary link between soil moisture and TB.

Soil roughness is well known to complicate the interpretation of microwave radiometer data and reduce the sensitivity of TB to soil moisture (Choudhury et al., 1979; Newton and Rouse, 1980). As a result, Wang and Choudhury (1981) developed a tractable semi-empirical model (referred to as the HQN model) to simulate the random roughness impact, which is currently being used in the SMOS (Kerr et al., 2019) and SMAP (O'Neill et al., 2021a) algorithms. Compared to flat soil, periodic (e.g., sinusoidal) row structures, a common type of soil tillage used for cultivation purposes, are less likely to be correctly modeled as a quasi-specular surface with random roughness (Ulaby et al., 1986).

Apart from roughness, the vegetation canopy attenuates (absorbs and scatters) the soil emission and adds its own contribution to the overall emission, resulting in a noticeable reduction in the sensitivity of TB to soil moisture (Jackson et al., 1982). The tau-omega (τ-ω) model proposed by Mo et al. (1982) models the TB response of vegetation-covered soil. Optical depth τ and single scattering albedo ω characterize the vegetation extinction and scattering, defined as $\tau = \int_0^h \kappa_e dx$ and $\omega = \kappa_s/\kappa_e$, respectively, where extinction coefficient κ_e is the sum of absorption coefficient κ_a and scattering coefficient κ_s, and h is the canopy height. The τ is directly proportional to the vegetation water content (VWC, in kg/m^2) of the canopy, while the ω primarily depends on the type of vegetation (Mo et al., 1982).

The tau-omega model is essentially a zero-order solution of the radiative transfer equations where multiple scattering is neglected, with applicability and accuracy being widely evaluated (Gao et al., 2018; Li et al., 2020). Many retrieval algorithms have been developed based upon this practical model, e.g., the single channel algorithm (SCA, Jackson, 1993) and the dual channel algorithm (DCA, Njoku and Li, 1999; Njoku et al., 2003) for SMAP, the L-band microwave emission of the biosphere (L-MEB) model (Wigneron et al., 2007) for SMOS, the land parameter retrieval model (LPRM, Owe et al., 2001), and the multi-temporal dual channel algorithm (MT-DCA, Konings et al., 2016; Konings et al., 2017).

The advancement of satellite observations and retrieval algorithms has made global soil moisture maps available every three days or less with satisfactory accuracy. For example, according to an evaluation of the SMAP Level 2 Soil Moisture Passive (L2SMP) Version 8 using in-situ validation sites (O'Neill et al., 2021b), the SCA V-polarization (SCA-V) and the DCA had the same best overall performance of ~0.036 m^3/m^3 in unbiased root-mean-square error (ubRMSE), fulfilling the 0.04-m^3/m^3 target accuracy of SMAP. However, the DCA showed better ubRMSE than the SCA at two agricultural sites. Consequently, the DCA has been adopted as the SMAP baseline algorithm since October 2021 (O'Neill et al., 2021a), with the SCA-V having been the baseline algorithm from the launch of SMAP (Chan et al., 2016).

Despite the above-mentioned achievements, global soil moisture sensing is still facing a few challenges. First, the moisture retrieval depth of the current L-band missions is believed to be 5 cm or even shallower (Escorihuela et al., 2010; Liu et al., 2012; Zheng et al., 2019), which limits direct application of the data in disciplines that require deeper soil moisture information, e.g., weather prediction and climate research. Second, the accuracy of these satellite products varies for different land surfaces. As an example, although the SMAP radiometer-based soil moisture data meets its overall target accuracy, errors for croplands are considerably larger (Chan et al., 2016; Colliander et al., 2017; Walker et al., 2019). Third, current SMAP and SMOS algorithms do not specifically consider any correction of the periodic row structure because of the lack of global information on temporally varying row shape, height, and orientation. In addition, there is currently no basis for how to upscale such field information to satellite footprint scales.

P-band (0.3–1 GHz/100–30-cm wavelength) is a promising candidate for conquering some of the difficulties faced at L-band due to its longer wavelength. It is a widely held understanding that a longer waveband should have a deeper moisture retrieval depth and reduced impact from surface roughness and vegetation (Ulaby et al., 1986), resulting in a more useful contributing depth and an overall higher soil moisture retrieval accuracy over vegetated rough/periodic soil surfaces. Accordingly, a recent P-band radar study known as the Airborne Microwave Observatory of Subcanopy and Subsurface (AirMOSS), has been conducted for retrieving root-zone soil moisture and moisture profiles (Tabatabaeenejad et al., 2014; Crow et al., 2018; Tabatabaeenejad et al., 2020). Alemohammad et al. (2019) concurrently collected P- and L-band backscatter observations using AirMOSS and the NASA/JPL's Uninhabited Aerial Vehicle SAR (UAVSAR), respectively, and demonstrated reduced vegetation scattering at P-band. In addition, P-band satellite signals of opportunity has been proven to have a potential for sensing subsurface soil moisture (Yueh et al., 2020). These findings have motivated a spaceborne P-band-radar mission for mapping global forest biomass, i.e., Biomass (Le Toan et al., 2011) scheduled for launch in 2023, and the SigNals of Opportunity: P-band Investigation (SNoOPI) for soil moisture mapping scheduled for launch in early 2022 (Garrison et al., 2021).

In terms of microwave radiometry, no observational evidence has been reported to demonstrate the postulated benefits of using P-band TB observations until the P-band Radiometer Inferred Soil Moisture (PRISM, see https://www.prism.monash.edu) project of Monash University. This project comprises a long-term tower experiment (2017–2021) and four airborne campaigns (2017, 2018, 2019, and 2021) to concurrently collect P- and L-band TB measurements over a range of roughness and vegetation conditions for investigating the potentially superior capability of a P-band radiometer over an L-band radiometer for soil moisture sensing. Taking advantage of the PRISM tower-based dataset, Shen et al. (2021) and Shen et al. (2022) have demonstrated a larger moisture retrieval depth and a reduced roughness impact at P-band compared to L-band over bare soil.

Following Shen et al. (2021) and Shen et al. (2022), this paper extends the investigation to wheat-covered soil with flat and periodic surfaces. For the first time, the tau-omega model was implemented at P-band to evaluate the vegetation effects at P- and L-band by comparing the retrieval errors before and after accounting for the wheat canopy in the forward model. Furthermore, the possibility of retrieving soil moisture over bare and wheat-covered soil without discriminating periodic and flat surfaces was investigated, by applying the roughness and vegetation parameters calibrated in flat soil to retrieve the soil moisture of periodic soil with the SMAP SCA and DCA. This demonstration suggests that an improved global soil moisture dataset may be possible using the longer wavelength P-band observations, even if the same algorithms as those of SMAP are used.

2. Experimental data

A tower-based site was established at Cora Lynn, Victoria, Australia (Fig. 1a) from October 2017 to May 2021, to investigate the potential of P-band radiometry in soil moisture remote sensing. The field was 160 m by 160 m in size and divided into four quadrants (Q1-Q4 from the northwest clockwise). A ten-meter-high tower was located at the center of the paddock (Fig. 1b), on which the two radiometers were installed, namely the Polarimetric P-band Multi-beam Radiometer (PPMR, Fig 1d) and the Polarimetric L-band Multi-beam Radiometer (PLMR, Fig. 1e). The PPMR and PLMR on the tower were rotated and tilted on a schedule so that they alternately observed the four quadrants at a variety of incidence angles (Fig. 1c).

PPMR and PLMR operate at dual linear (horizontal (H) and vertical (V)) polarizations (H- and V-pol), with 30° and 15° beamwidth, respectively. For a 40° incidence angle, the spatial resolution of the 3-dB

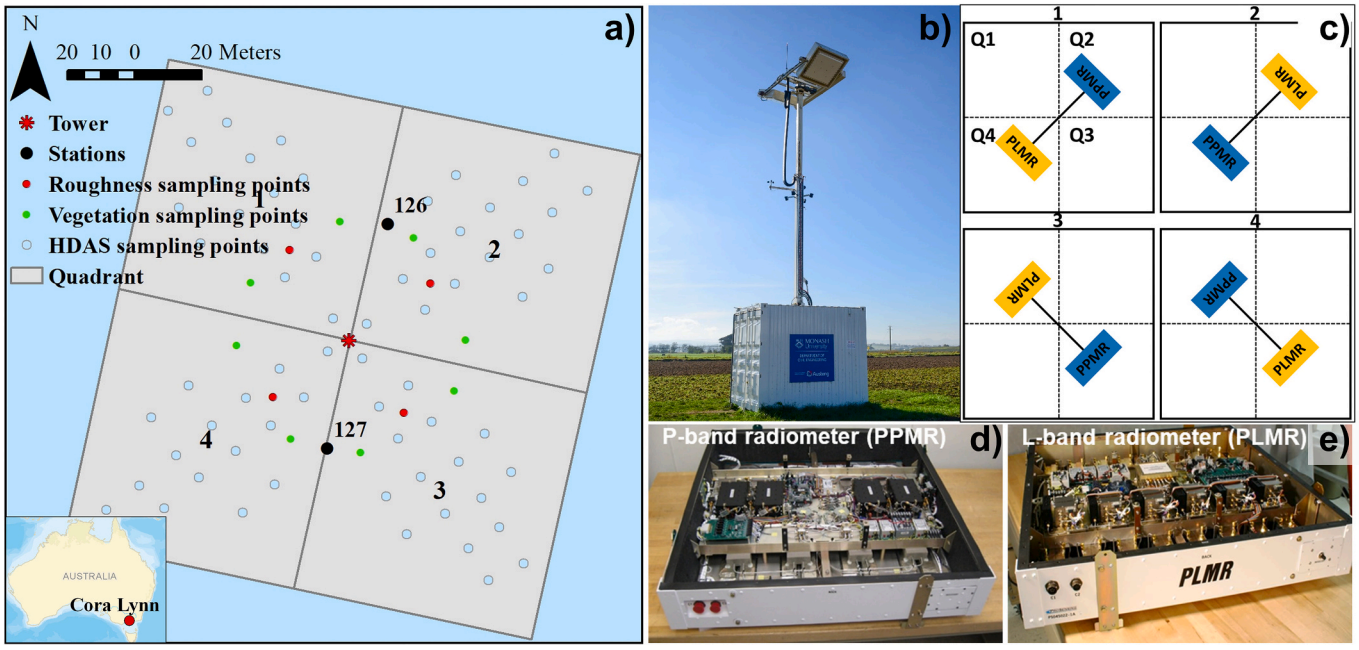

Fig. 1. Illustrations of the tower-based experiment at Cora Lynn, Victoria, Australia, including a) location map of the site; b) the tower carrying PPMR and PLMR; c) the four-step tower rotation cycle; d) PPMR operating at 0.742–0.752 GHz; and e) PLMR operating at 1.401–1.425 GHz.

footprints of PPMR and PLMR were approximately 8.2 × 7.0 m and 4.0 × 4.0 m, respectively. Both PPMR and PLMR have a calibration accuracy of better than 1.5 K; please refer to Shen et al. (2021) for more details about PPMR and PLMR. Unless otherwise noted, the terms "P-band" and "L-band" hereafter refer to the frequencies at which PPMR and PLMR operate.

Stations 126 and 127 (Figs. 1a and 2a) continuously recorded soil moisture and temperature at 5-cm intervals down to 60 cm, as shown in Fig. 2b. The top probe was installed vertically from the surface, while the others were installed horizontally (Fig. 2b). Fig. 2d shows how the spatial surface soil moisture (top ~5 cm) was measured at the locations shown in Fig. 1a using a system developed in-house, known as the Hydra-probe Data Acquisition System (HDAS, Merlin et al., 2007). These HDAS measurements were not used in the formal analysis but were used for checking the homogeneity of the soil moisture across the field and the representativeness of the stations. The hydra-probes used in this

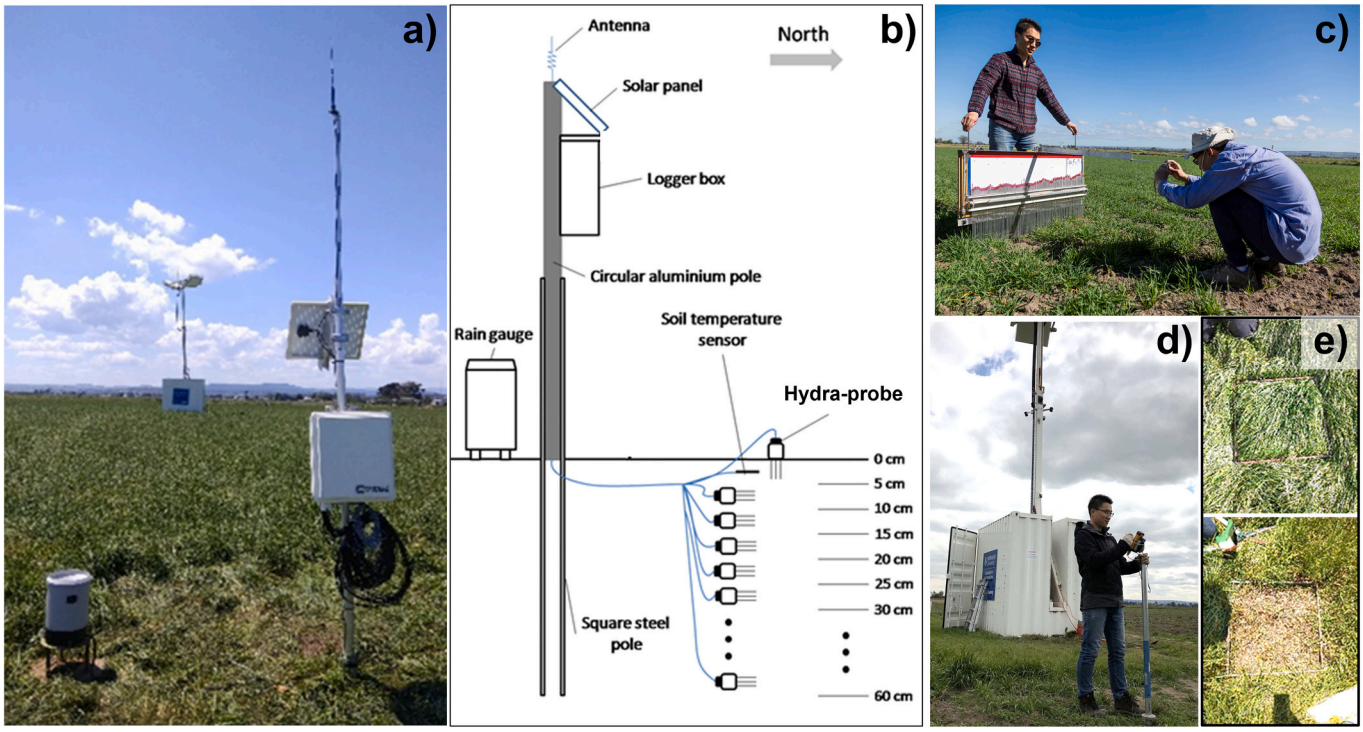

Fig. 2. Illustrations of the ground measurements, including a) station 126 monitoring soil moisture, temperature, and rainfall evolution; b) a diagram showing the station installation; c) soil surface roughness measurement with the pin-profiler; d) surface soil moisture measurement using HDAS; and e) an example of vegetation destructive sampling.

study were calibrated according to Merlin et al. (2007) and checked on-site using gravimetric samples. Soil texture samples obtained across the field were found to be a silt loam with 18.0% clay, 10.9% sand, and 71.1% silt. The soil bulk density of the surface soil layer in this site was 0.87 kg/m^3.

Quadrants 1–4 were plowed with varied roughness structures for the wheat-growing cycle from July to December 2019 to compare the random roughness of flat soil and the periodic roughness of furrowed soil (Fig. 3). Table 1 shows the roughness measurements taken during the whole wheat-growing period. On each sampling day, a pin-profiler with an ~0.5-cm pin interval was used to take three consecutive 1-m measurements (totaling 3-m) in two perpendicular directions in each quadrant (Fig. 2c). These roughness measurements were not used in the formal analysis but to support that the roughness parameters can be assumed constant over the entire study period.

Azimuth is the angle between the radiometer look direction and the row direction; period is the row spacing; and amplitude is half of the vertical distance between the bottom and the top of the row. For the periodic soil in Q1, Q3, and Q4, the roughness measurements across the rows were used to calculate the "periodic roughness" in the table, while those along the rows were used to calculate the "random roughness" in the table. For Q2, the measurements in two perpendicular directions were averaged to calculate the roughness statistics. Q3 and Q4 were plowed in one pass and had the same roughness structure (just different orientations relative to the tower look direction), and therefore the measurements in these two quadrants were averaged.

In this study, two periods in the entire wheat-growing cycle were used: 1) the bare soil period from July 17 to 31, 2019, before wheat germination (Fig. 3; top row) - details of this were presented by Shen et al. (2022); and 2) the wheat-covered soil period (Fig. 3; middle row) from November 13 to December 21, 2019, when matured wheat was senescing (a data example is plotted in Fig. 4). The current study used the daily TB observations at 40° incidence angle for P-band and at 38° incidence angle for L-band (Fig. 4a), in order to approximate the fixed 40° incidence angle of SMAP (Entekhabi et al., 2014). Moreover, Zhao et al. (2020) provide support by showing that 40° to 45° provided the best retrieval accuracy. Each of the TB observations in Fig. 4a was averaged from approximately 300 readings collected over a five-minute interval at around 6 am, because the soil temperature and dielectric profiles are likely to be more uniform at 6 am than other times of the day (Basharinov and Shutko, 1975). In addition, the difference between soil and canopy temperature is also minimized (Entekhabi et al., 2014).

Fig. 4b and c show the time series of soil moisture and temperature, respectively, collected from stations 126 and 127. This investigation follows the precedent of Shen et al. (2022) by using station 126 as the reference in Q2 and station 127 as the reference for Q1, Q3, and Q4 based on the agreement between HDAS measurements and the station soil moisture in flat and periodic quadrants respectively (Fig. 4b). The station observations were considered representative of the radiometer footprints because the HDAS measurements were relatively uniform across each quadrant and agreed with the corresponding station measurements (Fig. 4b). The destructive vegetation samples were taken weekly (Fig. 2e) at the locations shown in Fig. 1a. Accordingly, Fig. 4d presents the VWC measurements as boxplots and a fitted quadratic polynomial function to represent the VWC evolution.

While P-band was found to have a greater moisture retrieval depth (~7 cm) than L-band (~5 cm) over bare soil (Shen et al., 2021), given the difficulty in continuously measuring soil moisture at 5–7-cm depths, and the highly correlated soil moisture between neighboring layers, the daily mean soil moisture at around 6 am in the 0–5-cm layer from the station (Fig. 4b) was used for both P- and L-band evaluation in this paper.

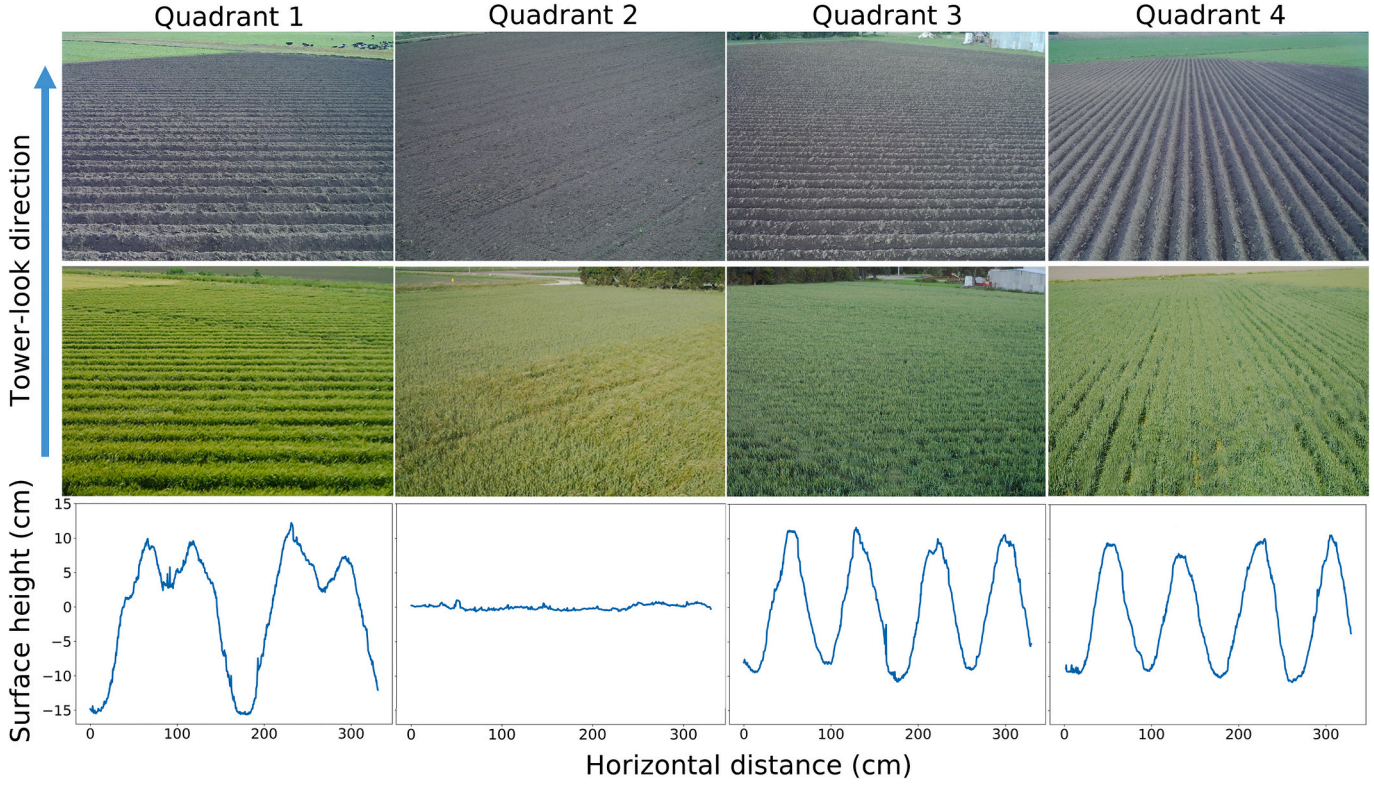

Fig. 3. Photos before the germination (top row) and at the maturity (middle row) of wheat, and diagrams of soil surface profiles (bottom row) of the four quadrants for the data used in this paper. Quadrants 3 and 4 were plowed in one pass and had the same roughness structures but with different orientations (perpendicular and parallel, respectively) relative to the tower look direction.

Table 1
Characterization of the roughness in the four quadrants.

Quadrant	Row structure	Periodic roughness				Random roughness		
		No. of profiles	Azimuth (°)	Period (cm)	Amplitude (cm)	No. of profiles	RMS height (cm)	Correlation length (cm)
1	Sinusoidal bench	6	90	165	10.5 ± 1.3	6	1.1 ± 0.5	9.2 ± 4.3
2	Flat	–	–	–	–	16	0.9 ± 0.2	9.5 ± 2.7
3	Sinusoidal	7	90	80	9.8 ± 1.2	7	0.8 ± 0.3	9.0 ± 4.2
4	Sinusoidal	7	0			7		

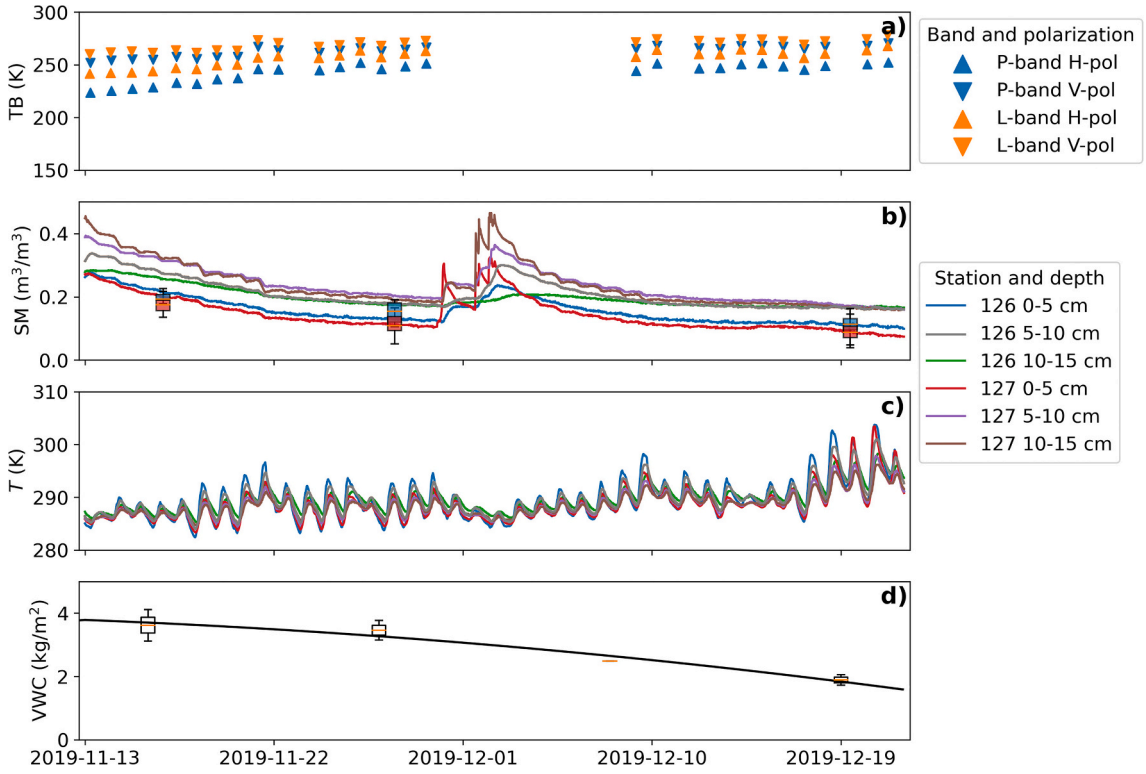

Fig. 4. Collected data including a) TB observations at 6 am in Q1 as an example, with the data gaps resulting from the tower being lowered due to high wind on those days; b) station time-series soil moisture with HDAS measurements (boxplots); c) station time-series soil temperature; and d) observed (boxplots) with fitted (black line) vegetation water content in Q1 as an example. For clarity only the data collected from the top 3 sensors are plotted in b) and c). Corresponding to the soil moisture evolutions of station 126 (in blue) in Q2 and station 127 (in red) in Q1, 3 and 4, the blue and red boxplots in b) show the maximum, 75% percentile, median, 25% percentile, and minimum of the spatial HDAS measurements in Q2 as well as Q1, 3 and 4, respectively. (For interpretation of the references to colour in this figure legend, the reader is referred to the web version of this article.)

3. Forward model

The well-known tau-omega model (Mo et al., 1982) characterizes the brightness temperature of the thermal emission (TB_P, where subscript P denotes either H- or V-pol) from a vegetated soil surface with four terms, i.e., 1) the direct upward emission from vegetation ($TB_P^{v\_up}$); 2) the downward vegetation emission reflected by the soil and attenuated by the canopy layer ($TB_P^{v\_down}$); 3) the upward soil emission attenuated by the canopy layer (TB_P^{s}), and 4) the downwelling sky emission (TB^{sky_down}) reflected by the soil and attenuated twice by the canopy layer (TB_P^{sky}), formulated as (Ulaby et al., 2014)

$$\begin{aligned} TB_P &= TB_P^{v\_up} + TB_P^{v\_down} + TB_P^{s} + TB_P^{sky} \\ &= (1-\omega)(1-\gamma_P)T_{eff}^{v} + (1-\omega)(1-\gamma_P)\gamma_P\Gamma_P T_{eff}^{v} + (1-\Gamma_P)\gamma_P T_{eff}^{s} \\ &\quad + TB^{sky\_down}\Gamma_P\gamma_P^2, \end{aligned} \tag{1}$$

where γ_P and T_{eff}^{v} are the transmissivity and effective temperature of the vegetation canopy, and Γ_P and T_{eff}^{s} are the reflectivity and effective temperature of the soil. The T_{eff}^{v} was assumed to be equal to the physical soil temperature in the 0–5-cm layer because the difference between canopy and soil temperature is minimal at 6 am (Fagerlund et al., 1970). Moreover, TB^{sky_down} was assumed to be constant and calculated to be 13.9 K at P-band and 5.3 K at L-band (ITU, 2015). The γ_P was computed from the optical depth τ_P using Beer's law such that

$$\gamma_P = exp\left[-\frac{\tau_P}{cos(\theta)}\right]. \tag{2}$$

For bare soil, Eq. (1) can be simplified to

$$TB_P = TB_P^{s} + TB_P^{sky} = (1-\Gamma_P)T_{eff}^{s} + TB^{sky\_down}\Gamma_P, \tag{3}$$

where Γ_P can be computed using the HQN model (Choudhury et al., 1979; Wang and Choudhury, 1981; Prigent et al., 2000)

$$\Gamma_P = \left[(1-Q_R)\Gamma_P^{*} + Q_R\Gamma_Q^{*}\right] exp\left[-H_{RP}cos^{N_{RP}}(\theta)\right], \tag{4}$$

where Γ_P^{*} is the specular reflectivity calculated from the Fresnel equations as a function of the relative soil dielectric constant ε_r ($\varepsilon_r = \varepsilon_r' - j\varepsilon_r''$), including real ($'$) and imaginary ($''$) parts, such that

$$\Gamma_H^* = \left| \frac{cos(\theta) - \sqrt{\varepsilon_r - sin^2(\theta)}}{cos(\theta) + \sqrt{\varepsilon_r - sin^2(\theta)}} \right|^2 \quad (5)$$

$$\Gamma_V^* = \left| \frac{\varepsilon_r cos(\theta) - \sqrt{\varepsilon_r - sin^2(\theta)}}{\varepsilon_r cos(\theta) + \sqrt{\varepsilon_r - sin^2(\theta)}} \right|^2. \quad (6)$$

The dielectric constant was related to soil moisture in this paper by the model of Mironov et al. (2013b), given that it accounts for the interfacial (Maxwell-Wagner) relaxation of soil water at P-band. This model neglects temperature dependence on the dielectric constant by assuming a constant temperature of 20 °C. Since the soil temperature was close to 20 °C at 6 am for most days of the study period (Fig. 4c), and that the dielectric constant of moist soil does not change substantially from 10 to 30 °C (Wagner et al., 2011), it is believed that using this model was reasonable for this research rather than the one developed specifically for SMOS at L-band (Mironov et al., 2013a). In this current investigation, the daily mean soil moisture at around 6 am in the 0–5-cm layer from the station (Fig. 4b) was used to simulate TB and evaluate the retrieved soil moisture at both P- and L-band.

According to radiative transfer theory, T_{eff}^s can be computed as (Choudhury et al., 1982)

$$T_{\text{eff}}^s = \int_0^\infty T(z)\alpha(z)exp\left[- \int_0^z \alpha(z')dz' \right] dz, \quad (7)$$

where $T(z)$ is the soil temperature at depth z, and $\alpha(z)$ is the power absorption coefficient depending on the soil dielectric constant ε_r and the observation wavelength λ written as (Ulaby et al., 1986)

$$\alpha(z) = 2 \bullet (2\pi/\lambda) \bullet \left| \text{Im}\left[\sqrt{\varepsilon_r(z)} \right] \right|, \quad (8)$$

where Im[ ] represents the imaginary part. In this paper, the effective soil temperature was calculated using Eqs. (7) and (8), as well as the soil moisture and temperature measurements. The soil was modeled as a semi-infinite medium, with the soil moisture and temperature below 60 cm assumed to be the same as those observed in the 55–60-cm layer.

4. Methodology

Given that the same mono-angular configuration as SMAP (~40°) was adopted in this research, the SMAP SCA and DCA approaches were implemented to evaluate the tau-omega model over bare and wheat-covered flat and periodic soil surfaces at P- and L-band. Additional to applying the default SMAP parameters to the soil moisture retrieval, roughness and vegetation parameters were locally calibrated in Q1-Q4 by feeding the forward model with coincident TB and soil moisture measurements. Subsequently, the calibrated parameters over the flat soil (Q2) were applied to the soil moisture retrieval over the periodic soil surfaces (Q1, Q3 and Q4), taking Q2 as calibration data and Q1, Q3 and Q4 as validation data. Finally, the retrieval performance for Q1, Q3 and Q4 was compared to Q2 as a benchmark.

Roughness and vegetation parameters can compensate for each other and thus cannot be calibrated together to achieve a robust result (Njoku and Chan, 2006; Patton and Hornbuckle, 2012; Martens et al., 2015). To disentangle roughness and vegetation effects, Wigneron et al. (1995) separately calibrated roughness and vegetation parameters by using the data before and after the vegetation canopy development, respectively. A similar methodology was also employed in this research. The roughness parameters calibrated over the bare soil period were therefore applied to the wheat-covered soil period because the surface roughness was found to have little change throughout the entire period, as indicated by the small standard deviation in Table 1.

Table 2
The default SMAP SCA parameters for croplands (O'Neill et al., 2021a).

Parameter	Value
H_R	0.108
Q_R	0
N_{RP}	2
b	0.11
ω	0.05

4.1. SCA

The SCA (Jackson, 1993) retrieves soil moisture using the TB observation at either H- or V-pol with all roughness and vegetation parameters known (Table 2). The b in Table 2 is an empirical parameter that builds a linear relationship between τ and VWC (Jackson and Schmugge, 1991), and thus τ can be estimated from

$$\tau = b \bullet \text{VWC}. \quad (9)$$

As in the SMAP SCA (O'Neill et al., 2021a), this research assumed the parameters in Table 2 were invariant throughout the study period.

Inversion of the forward model used the SLSQP (Sequential Least SQuares Programming, Kraft, 1988) algorithm to iteratively minimize a cost function (CF) computed from the differences between the observed TB (TB_P^{obs}) and the simulated TB (TB_P) at either H- or V-pol, expressed as

$$\text{CF} = \left(\text{TB}_P^{\text{obs}} - \text{TB}_P \right)^2. \quad (10)$$

The initial value of soil moisture was set to zero to avoid any potentially misleading prior knowledge in the retrieval. A bound of 0–1 m^3/m^3 was imposed on the retrieved soil moisture to ensure reasonable values were obtained.

4.2. DCA

The DCA (Njoku and Li, 1999; Njoku et al., 2003) uses dual-pol TB observations to retrieve two parameters. Unlike the SCA, the SMAP DCA uses a global map of H_R to concurrently retrieve soil moisture and τ. The H_R values vary from pixel to pixel, so no specific H_R value can be referred to in this paper. In addition, while N_{RP} is assumed to be 2 as in the SCA, Q_R is no longer assumed to be a constant value. Accordingly, H_R and Q_R were calibrated locally in Q1-Q4 using the bare soil data prior to undertaking retrieval. Afterward, soil moisture and τ were concurrently retrieved using the dataset for the wheat-covered period and the calibrated H_R and Q_R in Q2. The ω was assumed to be the same as in the SMAP DCA for both P- and L-band, being 0.6.

The CF minimized by the SLSQP algorithm using dual-pol TB at ~40° incidence angle during the retrieval period was

$$\text{CF} = \left(\text{TB}_H^{\text{obs}} - \text{TB}_H \right)^2 + \left(\text{TB}_V^{\text{obs}} - \text{TB}_V \right)^2 + \frac{\left(\tau^{\text{ini}} - \tau \right)^2}{\sigma(\tau)^2}, \quad (11)$$

where τ^{ini} and τ are the initial and retrieved values of the optical depth, and $\sigma(\tau)$ is the parameter to balance the weight of the retrieved parameters for the optimization process to converge. The initial values of soil moisture and τ were set to zero. The same $\sigma(\tau)$ value as in the SMAP DCA was adopted, i.e., 0.05 (O'Neill et al., 2021a).

5. Results

5.1. SCA – the HQN model for bare soil

Since Shen et al. (2022) found that the default SMAP parameters cannot fully account for the periodic roughness impact, especially at L-band, the H_R values were calibrated using the bare soil data (Fig. 5). A

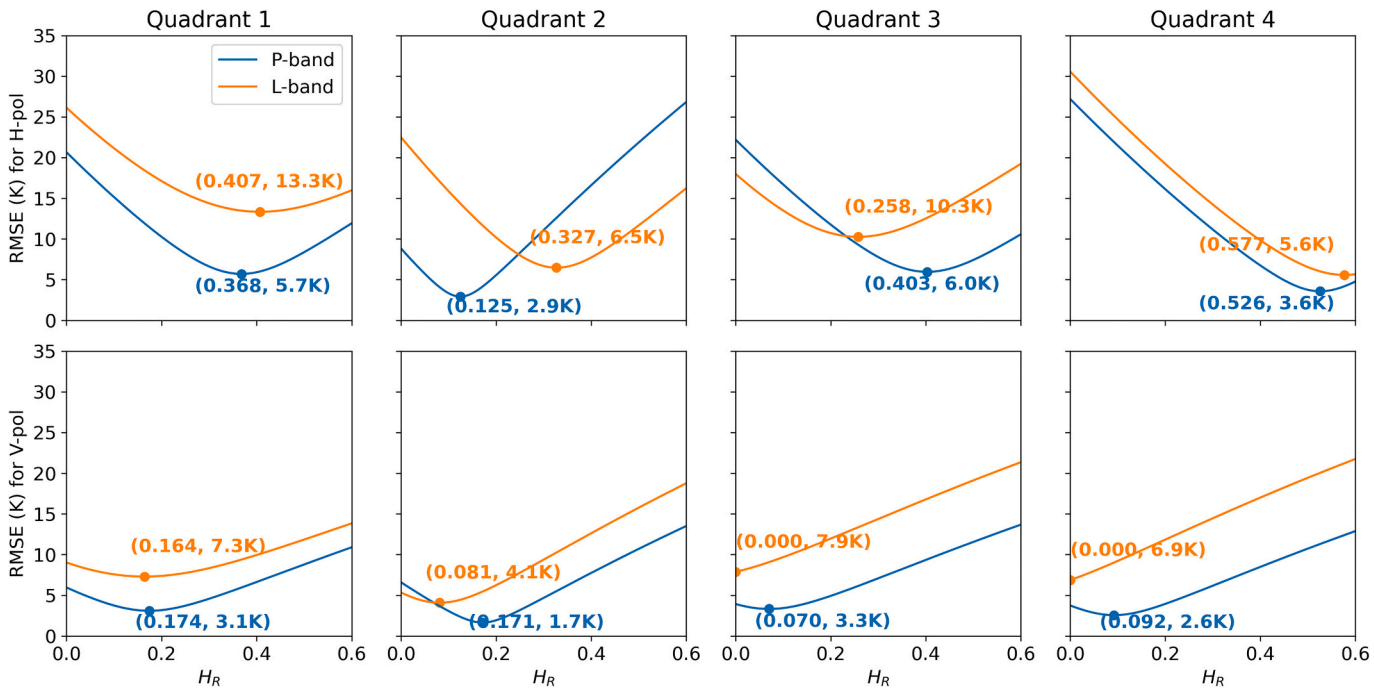

Fig. 5. RMSE (K) between the observed and simulated TB using a range of H_R values at H-pol (top row) and V-pol (bottom row) over the bare soil in each quadrant. The model for bare soil (Eq. (3)) was adopted as the forward model. The dots with values indicate the minimum RMSE and the corresponding H_R values for P-band (in blue) and L-band (in orange). The parameters Q_R and N_{RP} were assumed to be the same as in the SMAP SCA at both P- and L-band, being 0 and 2, respectively. (For interpretation of the references to colour in this figure legend, the reader is referred to the web version of this article.)

range of H_R values were used to simulate the TB for P- and L-band and H- and V-pol respectively using the bare soil model (Eq. (3)). The H_R values that produced the minimum RMSE between the simulated and observed TB were considered the optimum, marked as the dots with annotated values in Fig. 5.

Compared to L-band, the HQN model performed better at P-band based on its lower RMSE. For example, the minimum RMSE in Q1 and Q3 was no higher than 6 K at P-band, while that at L-band was higher than 10 K. Moreover, at L-band V-pol, the RMSE in Q3 and Q4 was a minimum at $H_R = 0$ and will further decrease if negative H_R is allowed. These phenomena can be attributed to the substantial impact of periodic row structures and the inapplicability of the SMAP SCA configuration (i.

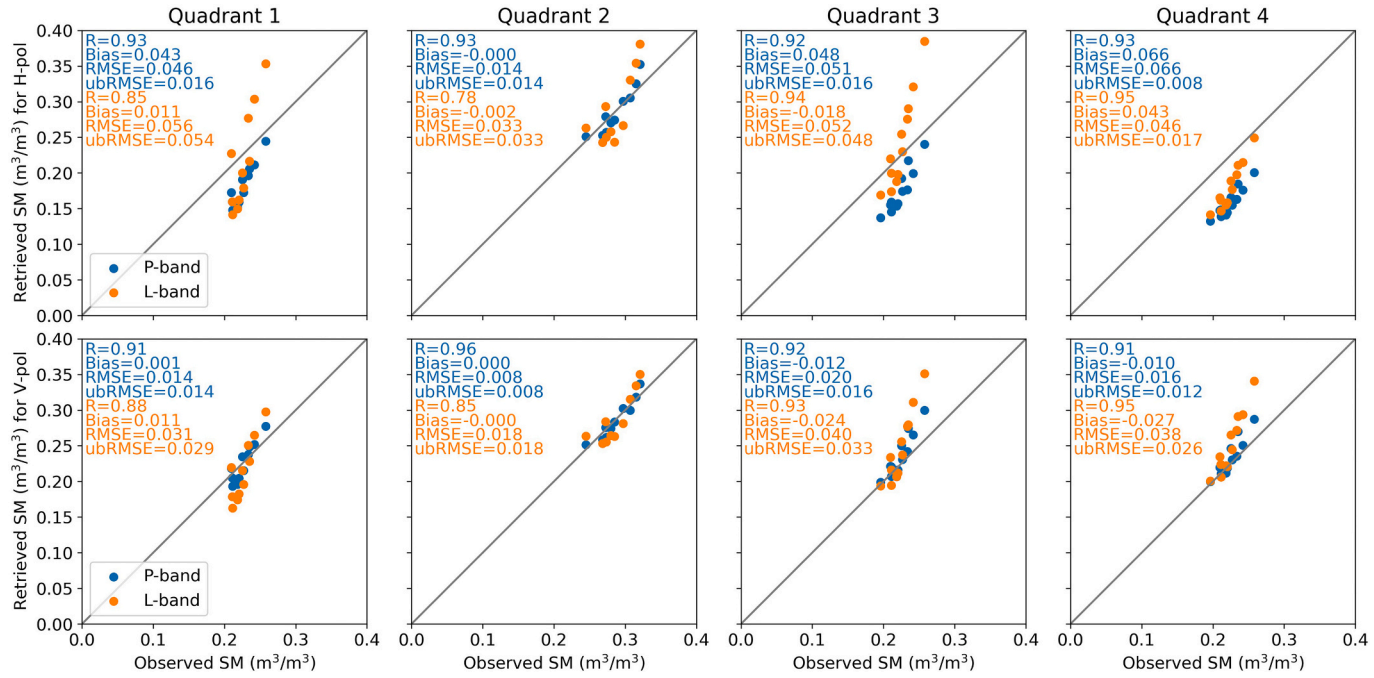

Fig. 6. Retrieved versus observed soil moisture for H-pol (top row) and V-pol (bottom row) over the bare soil in each quadrant, using the SCA (Eq. (10)) with the bare soil forward model (Eq. (3)). Calibrated H_R values from the period of bare flat soil in Q2 were used for all quadrants here, i.e., 0.125 and 0.171 for P-band H- and V-pol, respectively, and 0.327 and 0.081 for L-band H- and V-pol, respectively. The parameters Q_R and N_{RP} were assumed to be the same as those from the SMAP SCA at both P- and L-band, being 0 and 2, respectively.

e., $Q_R = 0$ and $N_{RV} = 2$) for periodic roughness at L-band. For both P- and L-band and both H- and V-pol, Q2 had the lowest calibration residual across the four quadrants with only one exception (L-band H-pol in Q4), indicating the more considerable roughness impact of periodic surfaces than from the flat surface in Q2. Importantly, the H_R in the four quadrants was more comparable at P- than L-band at V-pol, with the standard deviation being 0.046 and 0.068, respectively.

To evaluate the induced retrieval error from applying the calibrated H_R in flat soil to periodic soil, the optimal parameters calibrated in Q2 (Fig. 5) were used to retrieve the soil moisture in all four quadrants for both bands and both polarizations, with the comparison of the retrieved and observed soil moisture plotted in Fig. 6. As expected, Q2 was seen to have the best retrieval performance across all four quadrants because H_R was calibrated in Q2, which was done intentionally to get a benchmark accuracy that can be compared to for the other three quadrants with periodic soil surfaces. P-band was found to perform better than L-band in RMSE in all quadrants except Q4 for H-pol. In Fig. 6, V-pol had better retrieval accuracy than H-pol at both P- and L-band. Focusing on V-pol (Fig. 6 bottom row), P-band had similar RMSEs across all four quadrants, whereas L-band showed higher RMSE over periodic soil (0.031–0.040 m^3/m^3) than that over flat soil (0.018 m^3/m^3), indicating the reduced roughness impact at P-band.

5.2. SCA – the tau-omega model for wheat-covered soil

The default SMAP SCA parameters for croplands (Table 2) were evaluated at P- and L-band and H- and V-pol over the wheat-covered soil with different roughness structures using the tau-omega model (Eq. (1)), with the simulated and observed TB compared in Fig. 7. L-band was found to substantially outperform P-band in all cases, indicating the inapplicability of the default SMAP SCA parameters (Table 2) at P-band. Similar to Figs. 5 and 6, Fig. 7 also shows a superior performance at V- over H-pol. More specifically, the RMSE at L-band was no higher than 3 K at V-pol, demonstrating that the default SMAP SCA parameters were applicable to a wide range of roughness and vegetation conditions with satisfactory accuracy. In the following, only V-pol was analyzed due to its superiority over H-pol according to Figs. 6 and 7.

The SMAP SCA parameters were demonstrated to work very well at L-band with low RMSE shown in Fig. 7, and therefore only the vegetation parameters (b and ω) at P-band were calibrated in Fig. 8. The soil moisture measurements collected over the wheat-covered soil were adopted to simulate TB, using the tau-omega model with calibrated H_R (Fig. 5) and varying b and ω. Overall, the b and ω values differed slightly across quadrants, ranging from 0.099 to 0.150 and from 0.119 to 0.137, respectively (Fig. 8). The varied b and ω can be partially attributed to the different residuals of the roughness calibration (Fig. 5) that were left to be compensated by b and ω. Comparing the default and calibrated parameters, ω differed more considerably than other parameters, being 0.05 in the default configuration (Table 2) and ~ 0.12–0.13 after calibration (Fig. 8).

The minimum RMSE was no higher than 2 K, indicating a good performance of the tau-omega model over the wheat-covered random and periodic soil. Additionally, even though the b and ω values denoted by the yellow circles in Fig. 8 are technically the calibrated parameters, a range of adjacent values can still be used if a certain calibration residual (e.g., 2 K) is tolerated.

Soil moisture was subsequently retrieved at P- and L-band V-pol using the tau-omega model (Fig. 9). While the roughness (Fig. 5) and vegetation (Fig. 8) parameters were calibrated at P-band in all four quadrants, only the parameters calibrated in Q2 ($H_R = 0.171$, $b = 0.099$, and $\omega = 0.134$) were used for the soil moisture retrieval at P-band (Fig. 9). At L-band, the SMAP SCA parameters (Table 2) were applied to the soil moisture retrieval (Fig. 9). It can be seen from Fig. 9 that the RMSEs/ubRMSEs were similar across all four quadrants either at P- or L-band (variations no more than 0.016 m^3/m^3), suggesting the possibility to ignore the different roughness structures underneath vegetation when retrieving soil moisture.

5.3. DCA

Before applying the DCA soil moisture retrieval to the vegetated period, the full-time-series TB and soil moisture during the bare soil period were used to calibrate the roughness parameters, i.e., H_R and Q_R at P- and L-band in each quadrant, shown in Fig. 10. The H_R and Q_R values that produced the minimum RMSE were considered as the calibrated values, marked as the yellow circles with annotated values in

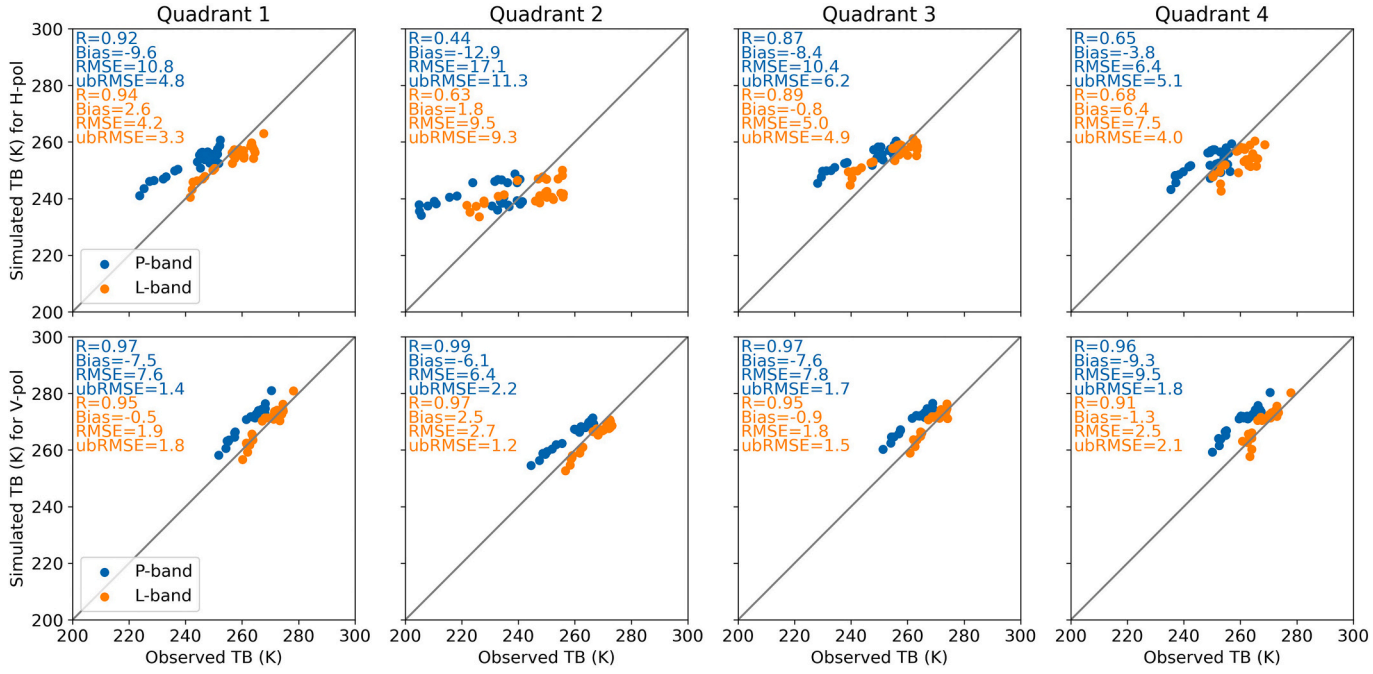

Fig. 7. Comparison of TB simulations against observations for H-pol (top row) and V-pol (bottom row) over the wheat-covered soil in each quadrant, using the SCA (Eq. (10)) with the tau-omega model (Eq. (1)). The default SMAP SCA parameters in Table 2 were used for all quadrants, both bands, and both polarizations.

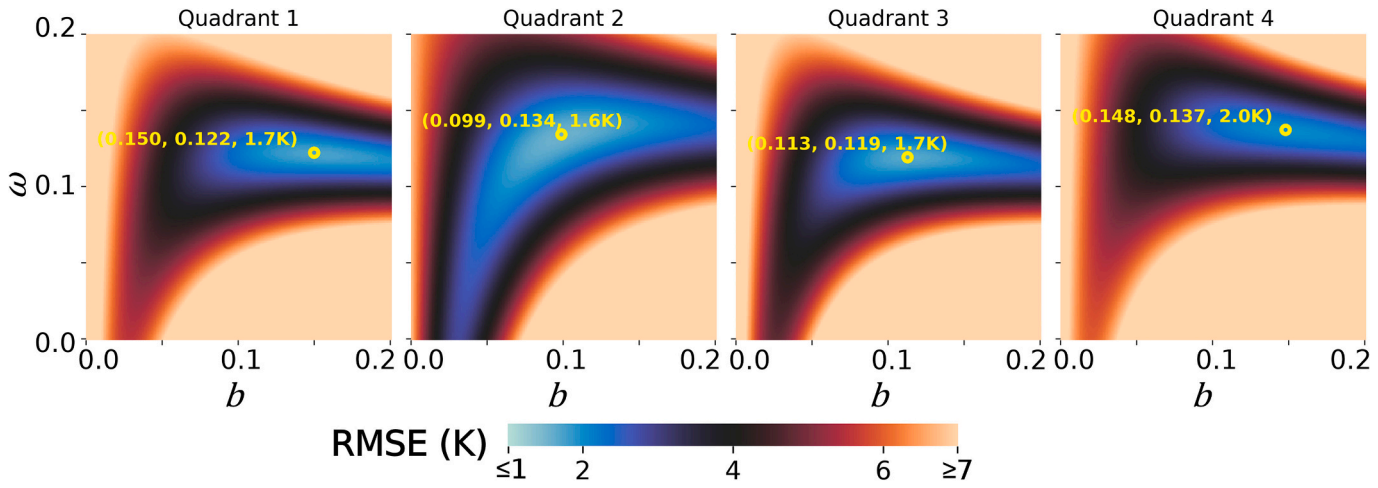

Fig. 8. RMSE (K) between the observed and simulated TB using a range of b and ω values for P-band V-pol over the wheat-covered soil in each quadrant. The tau-omega model (Eq. (1)) was adopted as the forward model. The yellow circles indicate where the minimum RMSE was reached, with the three values showing b, ω, and the minimum RMSE, respectively. The calibrated H_R values at P-band V-pol from the period of bare soil, i.e., 0.174, 0.171, 0.070, and 0.092, were used for Q1-Q4, respectively. The parameters Q_R and N_{RP} were assumed to be the same as in the SMAP SCA, being 0 and 2, respectively. (For interpretation of the references to colour in this figure legend, the reader is referred to the web version of this article.)

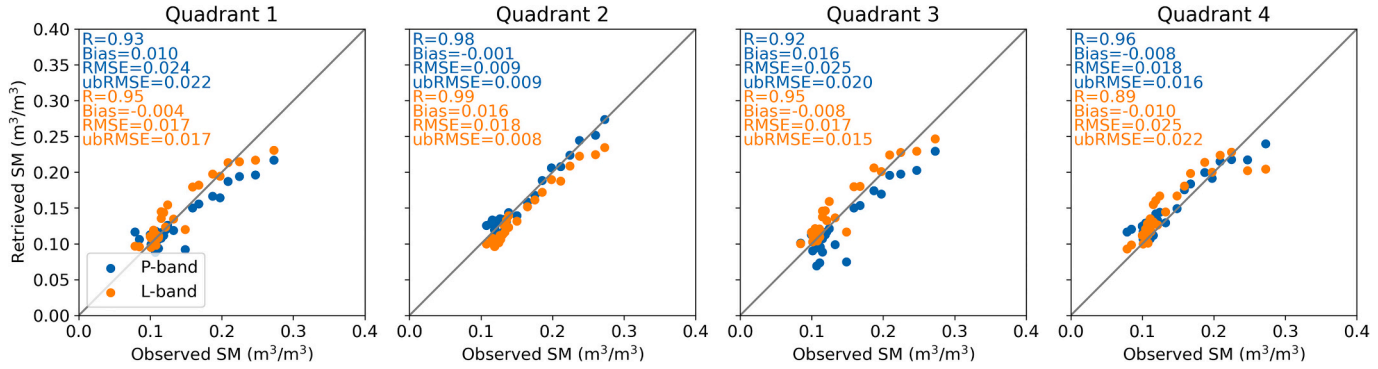

Fig. 9. Observed versus retrieved soil moisture over the wheat-covered soil in each quadrant, using the SCA-V (Eq. (10)) with the tau-omega model (Eq. (1)). The default SMAP SCA Q_R and N_{RP} and the calibrated H_R, b, and ω parameters in Q2 (flat soil) were used for P-band in all quadrants here, i.e., $Q_R = 0$, $N_{RP} = 2$, $H_R = 0.171$, $b = 0.099$, and $\omega = 0.134$. The default SMAP SCA parameters in Table 2 were used for L-band in all quadrants.

Fig. 10.

Similar to Fig. 5, Fig. 10 also shows a lower RMSE at P- than L-band in the four quadrants, being 2.6–4.8 K and 5.4–10.8 K, respectively. This indicates that the HQN model performs better at P-band due to the reduced roughness impact. Q2 had the lowest calibration residual across the four quadrants for both P- and L-band because of its relatively smooth surface compared to the periodic soil surfaces in Q1, Q3 and Q4. While Q_R is usually assumed to be zero (e.g., Wigneron et al., 2001; Martens et al., 2015), this assumption was only found to be valid at P-band but not at L-band in Q2 when using dual-pol TB, confirming the studies with non-zero Q_R values at L-band (e.g., Lawrence et al., 2013). Moreover, Fig. 10 supports that non-zero Q_R should apply for periodic surfaces when performing a DCA retrieval. It is also worth noting that H_R and Q_R were larger in Q4 than Q3, particularly at L-band, indicating that the periodic surface with parallel structures might have a larger impact than that with perpendicular structures at ~40° incidence angle, in spite of the same row spacing and height.

Fig. 11 presents the comparison of the observed and retrieved soil moisture when applying the H_R and Q_R calibrated in Q2 (Fig. 10) to all four quadrants. P-band was found to perform better than L-band in all metrics. Similar to the SCA result in Fig. 9, the RMSEs and ubRMSEs shown in Fig. 11 at either P- or L-band were comparable across the four quadrants, with variations of no more than 0.011 m^3/m^3.

While the SMAP baseline algorithm has recently changed to the DCA from the SCA-V due to the improved performance in some agricultural areas (O'Neill et al., 2021b), based on Figs. 9 and 11 in this research, the DCA showed higher RMSE (e.g., 0.028 m^3/m^3 at P-band and 0.062 m^3/m^3 at L-band in Q2) than the SCA-V (e.g., 0.009 m^3/m^3 at P-band and 0.018 m^3/m^3 at L-band in Q2). These results are consistent with the earlier validation results of SMAP (Chan et al., 2016).

5.4. Estimation of vegetation impact

To investigate whether P-band had a reduced vegetation impact at P-band, the soil moisture was retrieved over the wheat-covered soil in Q2 without considering the vegetation impact in the model (Fig. 12), i.e., using the bare soil model (Eq. (3)) with the calibrated H_R parameters in Fig. 5, being 0.171 for P-band and 0.081 for L-band. P-band was found to outperform L-band substantially in RMSE, being 0.029 and 0.063 m^3/m^3 for P- and L-band, respectively. The default SMAP H_R values for the SCA (0.15 for bare soil and 0.108 for croplands) were also investigated for both P- and L-band (not shown), and no discernable difference in RMSE was found compared to that in Fig. 12.

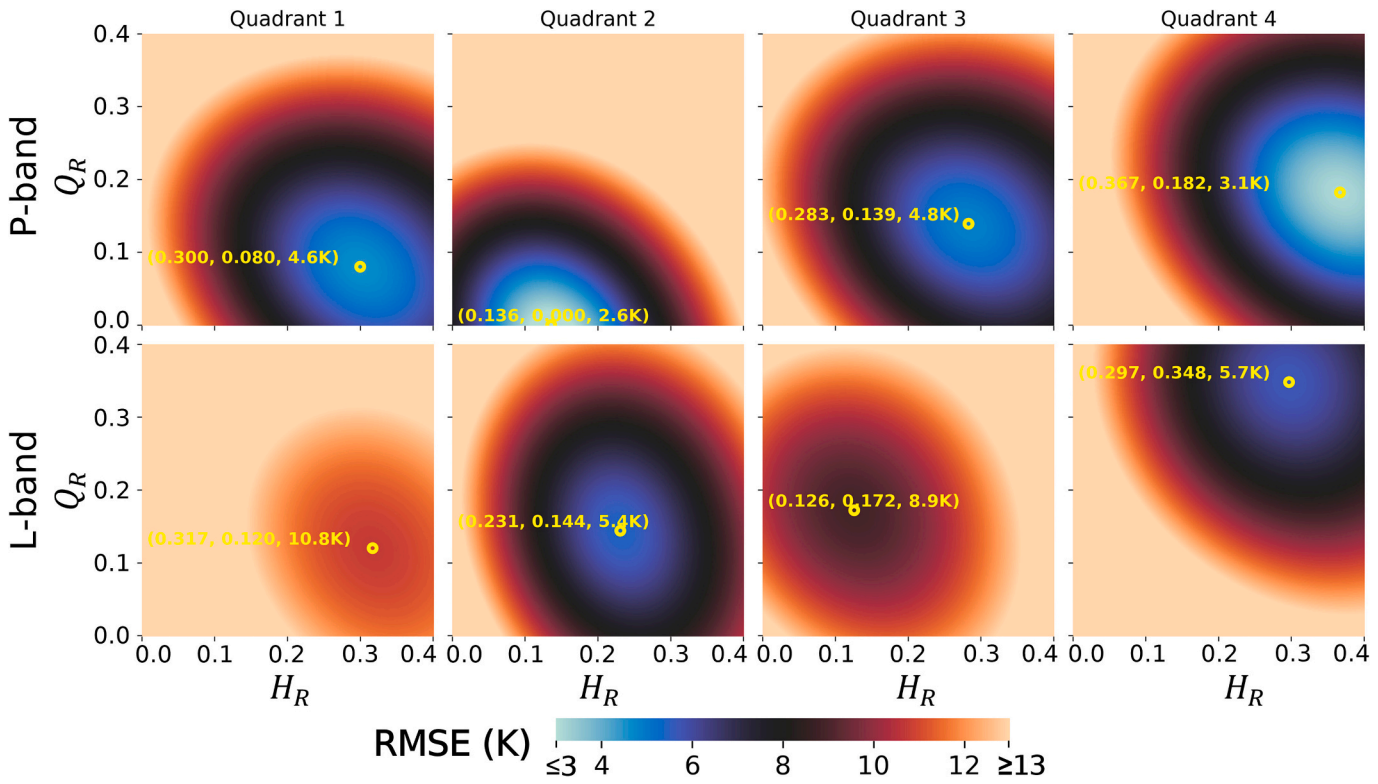

Fig. 10. RMSE (K) between the observed and simulated dual-pol TB using a range of H_R and Q_R values for P-band (top row) and L-band (bottom row) over the bare soil in each quadrant. The model for bare soil (Eq. (3)) was adopted as the forward model. The yellow circles indicate where the minimum RMSE was reached, with the three values showing H_R, Q_R, and the minimum RMSE, respectively. The N_{RP} was assumed to be 2, the same as in the SMAP DCA, at both P- and L-band. (For interpretation of the references to colour in this figure legend, the reader is referred to the web version of this article.)

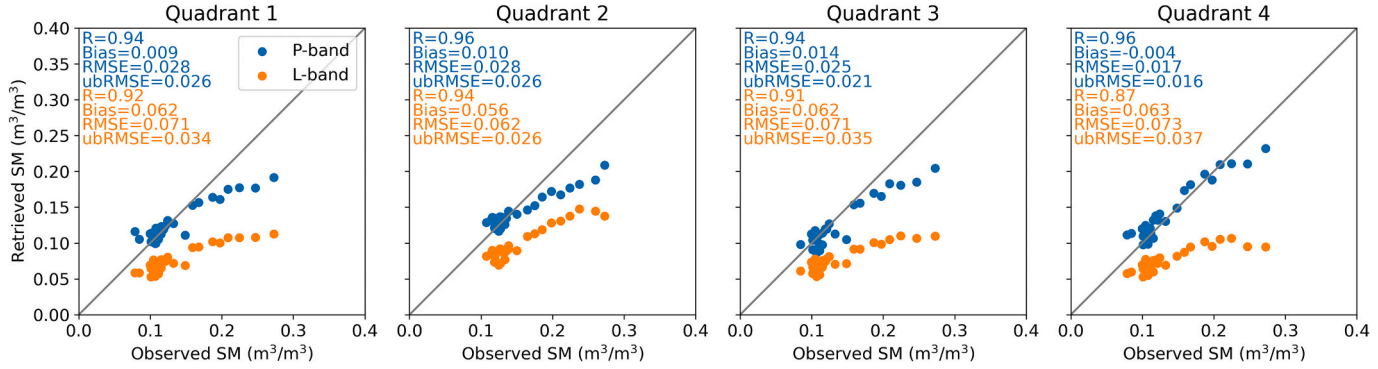

Fig. 11. Observed versus retrieved soil moisture over the wheat-covered soil in each quadrant, using the DCA (Eq. (11)) with the tau-omega model (Eq. (1)). The default SMAP DCA N_{RP} and ω were used for both P- and L-band, i.e., $N_{RP} = 2$ and $\omega = 0.06$. The calibrated H_R and Q_R from the period of bare flat soil in Q2 were used for all quadrants, i.e., $H_R = 0.136$ and $Q_R = 0$ for P-band and $H_R = 0.231$ and $Q_R = 0.144$ for L-band.

6. Discussion

6.1. Do periodic surfaces need to be discriminated in soil moisture retrieval at P- and L-band?

For the bare flat and periodic soil, the HQN model worked better at P- than L-band, supported by the lower RMSE at P-band in the simulation results of Figs. 5 and 9. In terms of soil moisture retrieval, P-band was also shown to have lower RMSE than L-band in Fig. 6. Shen et al. (2022) pointed out that the default SMAP and SMOS parameters induced larger errors over periodic surfaces than flat surfaces. In the current investigation, the H_R was calibrated in Q2 and then applied to retrieve the soil moisture in all four quadrants, with the result showing that P-band had a reduced error compared to L-band (Fig. 6). This evidence collectively confirms the conclusion by Shen et al. (2022) that P-band was less impacted by random and periodic roughness than L-band.

For the wheat-covered soil with different roughness structures, the default SMAP SCA parameters were found to work very well at L-band but not at P-band (Fig. 7). Moreover, the calibrated parameters at P-band led to an RMSE similar to that obtained at L-band using the default SMAP SCA parameters, being no higher than 3 K (Figs. 7 and 8). From the aspect of soil moisture retrieval, no substantial variation across different quadrants was observed at both P- and L-band whether using the SCA (Fig. 9) or the DCA (Fig. 11), indicating that the same parameters can be used for wheat-covered soil with different roughness structures.

In summary, P-band did not need to have the periodic surfaces discriminated for either bare or wheat-covered soil, while L-band

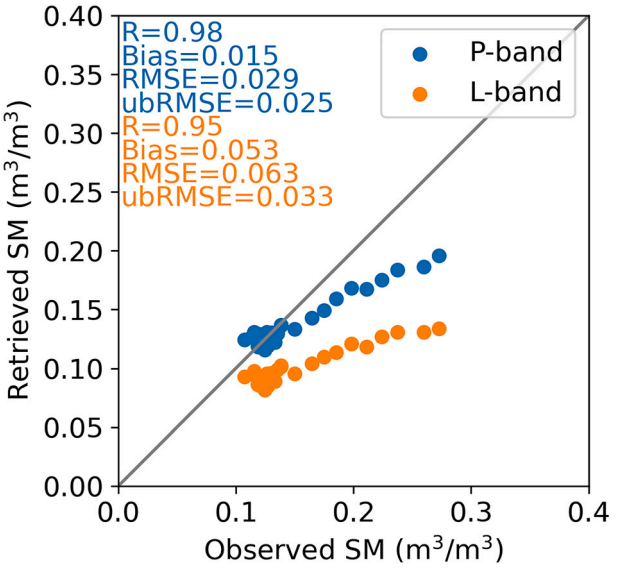

Fig. 12. Observed versus retrieved soil moisture over the wheat-covered soil in Q2, using the SCA-V (Eq. (10)) with the bare soil forward model (Eq. (3)). Calibrated H_R values from the period of bare flat soil in Q2 were used here, i.e., 0.171 for P-band and 0.081 for L-band, while Q_R and N_{RV} were assumed to be the same as those from the SMAP SCA at both P- and L-band, being 0 and 2, respectively.

needed differently calibrated parameters for bare periodic surfaces compared to bare flat surfaces due to the more considerable roughness impact. However, when the wheat canopy covered the soil, the periodicity of the surfaces no longer needed to be considered at L-band. A possible explanation is that the mature wheat canopy "masked" the roughness structures below.

6.2. *Can low-to-intermediate vegetation be omitted in soil moisture retrieval at P- and L-band?*

When using one TB observation to retrieve one soil moisture using the tau-omega model (i.e., the SCA), prior vegetation information (e.g., VWC, NDVI (Normalized Difference Vegetation Index), LAI (Leaf Area Index, Yadav et al., 2020), etc.) is required to estimate τ using Eq. (9). When such information is not available, the use of P-band observations can still achieve an acceptable performance (0.029 m^3/m^3 in RMSE) when completely ignoring the vegetation impact by using the bare soil model (Fig. 12). In contrast, the corresponding RMSE at L-band was as high as 0.063 m^3/m^3, demonstrating that the impact of low-to-intermediate vegetation (under 4 kg/m^2) can be neglected at P-band but not at L-band.

Neglecting the vegetation resulted in underestimating the soil moisture observations (Fig. 12) because the vegetation contribution was mistakenly considered as a soil contribution, increasing the soil emissivity and thus decreasing the soil moisture. This phenomenon was particularly prominent for high soil moisture (Fig. 12) when the VWC was also high (Fig. 4). Consequently, it can be postulated that the advantage of P- over L-band in reducing the vegetation impact will become more considerable when the VWC achieves a higher range, e.g., corn (Hornbuckle and England, 2004).

6.3. *Are model parameters comparable across different frequencies?*

Directly comparing the model parameters (i.e., H_R, Q_R, b, and ω) across different frequencies seems to be a straightforward way to judge the reduced roughness and vegetation impact at a specific frequency compared to others. However, this might not actually make sense. Gao et al. (2017) calibrated the H_R and b at L-, C- and X-band by assuming $\omega = 0.05$ and found H_R and b increased with increasing frequency. On the contrary, Wang et al. (1983) discovered that H_R did not have a definitive relation to frequency. While Mo et al. (1982) obtained higher H_R and b values at C-band than those at L-band, consistent with Gao et al. (2017), they found ω was higher at L-band, contradictory to microwave radiometry theory which suggests that a longer wavelength band should have reduced scattering effects. Additionally, considering the results in this paper (Figs. 5, 8, and 10) where no explicit frequency-dependence was found for the parameters H_R, b, and ω, it might be concluded that these model parameters should not be compared across different frequencies.

Two reasons can be attributed to the incomparability of those model parameters. First, the tau-omega and the HQN models are semi-empirical, approximating the rigorous physical process by linking the model parameters (i.e., H_R, b, and ω) to some measurable variables (e.g., rms height, correlation length, and VWC). Meanwhile, many assumptions have been made to develop simplified analytical equations, including the homogeneity of soil moisture in space and with depth, the scattering isotropy of soil and vegetation, and the negligibility of the high-order scattering. Therefore, these parameters have to be considered as effective rather than physical (Wigneron et al., 2017).

Second, the mismatch between the sampling depth of the soil moisture measurements and the theoretical moisture retrieval depth may also lead to an incomparability of model parameters. The moisture retrieval depth is dependent on frequency and moisture profile and is thus a time-variant variable (Shen et al., 2021), making it impractical to calibrate the model parameters using the soil moisture observations exactly within the moisture retrieval depth, let alone the challenge to measure the continuous soil moisture in a very thin layer, e.g., 1–2 cm.

The Q_R was found to be a possible exception from both the literature and current results when estimated to be non-zero. Fig. 10 presents that the Q_R values at P-band were lower than those at L-band in all four quadrants. Similarly, Wang et al. (1983) has reported that while H_R is not correlated to frequency, such a relation exists for Q_R, being 0.01, 0.15, and 0.20 at 1.4, 5, and 10.7 GHz, respectively, for a soil surface with 0.73-cm rms height. However, such a conclusion is drawn with much caution, given that relevant studies mostly assumed constant Q_R (e.g., Wigneron et al., 2001; Martens et al., 2015) and thus more evidence is still required.

6.4. *What are the challenges of a successful P-band-radiometer mission?*

While it has been demonstrated that P-band is a promising proposition to replace or enhance the current L-band SMOS and SMAP missions in the forthcoming years, so as to obtain deeper and more accurate soil moisture information (Shen et al., 2021; Shen et al., 2022), there remain four challenges: aperture size, radio frequency interference (RFI), receiver design and calibration, and ionospheric and celestial emission effects (Johnson et al., 2021).

With the spatial resolution of a radiometer determined by the size of the antenna relative to the observing wavelength for a given orbit altitude, the aperture of a 0.75-GHz radiometer needs to be enlarged by 1.87 times to retain the same 40-km spatial resolution of the 1.4-GHz radiometer of SMAP, i.e., increasing from the 6-m-diameter antenna of SMAP to an 11.22-m-diameter antenna. Moreover, unlike L-band (1.400–1.427 GHz) that is exclusively allocated for radio astronomy use, P-band (0.3–1 GHz) is heavily occupied by television broadcast, communications, and other applications (National Research Council, 2010), easily causing RFI and corrupting radiometric measurements from the target. Additionally, at 0.75 GHz, the amount of Faraday rotation and ionosphere-specific attenuation is approximately 3.5 times as large as at 1.4 GHz, which needs to be corrected.

Nowadays, large deployable antennas (e.g., Meguro et al., 2009) and highly developed downscaling techniques (Peng et al., 2017; Sabaghy et al., 2018; Sharma et al., 2021) make higher spatial resolution at P-band possible. Moreover, RFI mitigation techniques are becoming

increasingly mature (Skou et al., 2009; Huang et al., 2018; Jin et al., 2019). The ultra-wideband software defined microwave radiometer (UWBRAD) is a successful example in this regard for demonstrating how a future P-band-radiometer mission might address the RFI issue (Johnson et al., 2016; Yardim et al., 2021). The UWBRAD detects and filters RFI by segmenting the observed bandwidth (from 0.5 to 2 GHz) into 12 channels, each of which is further resolved into 512 subchannels, so that the RFI-free portions of the spectrum can be identified and integrated. These advancements in aerospace and remote sensing technologies pave the way for a successful P-band-radiometer mission in the near future.

7. Conclusion

This paper evaluated the tau-omega model over bare and wheat-covered flat and periodic surfaces at P- and L-band to demonstrate the potential improvement in soil moisture retrieval from using the longer wavelength P-band observations. For the bare flat and periodic soil surfaces, V-pol was less impacted by roughness impact than H-pol at both P- and L-band in terms of both TB simulation and soil moisture retrieval. Evaluating the SCA-V retrieval results showed that P-band had a more comparable RMSE than those at L-band across different roughness configurations, with variations being up to 0.012 and 0.022 m^3/m^3 for P- and L-band, respectively.

For the wheat-covered soil, the default SMAP SCA parameters for croplands were found to simulate TB satisfactorily at L-band V-pol but not at L-band H-pol or P-band. Therefore, at P-band V-pol, the roughness and vegetation parameters were calibrated in Q2 (flat soil) and applied to retrieve the soil moisture in all four quadrants, while the default SMAP parameters were applied to retrieve the soil moisture in all four quadrants at L-band V-pol. The RMSE between observed and retrieved soil moisture showed that neither P- or L-band had substantial performance variation across different quadrants for the SCA or DCA. However, the DCA had a degraded retrieval performance compared to the SCA-V.

In short, P-band had a reduced roughness impact and was thus able to model both the flat and periodic soil using the calibrated parameters from the flat soil, for both bare and wheat-covered soil. Conversely, L-band could only treat the different periodic surfaces like a flat surface when covered by a mature wheat canopy. Moreover, a lower RMSE at P-band (0.029 m^3/m^3) than L-band (0.063 m^3/m^3) was observed when omitting vegetation effects in the forward model, confirming that P-band observations were relatively unaffected by the wheat canopy.

CRediT authorship contribution statement

Xiaoji Shen: Conceptualization, Methodology, Formal analysis, Investigation, Data curation, Writing – original draft, Visualization. **Jeffrey P. Walker:** Conceptualization, Validation, Resources, Writing – review & editing, Supervision, Project administration, Funding acquisition. **Nan Ye:** Validation, Investigation, Data curation. **Xiaoling Wu:** Investigation, Data curation. **Foad Brakhasi:** Investigation, Data curation. **Nithyapriya Boopathi:** Investigation, Data curation. **Liujun Zhu:** Writing – review & editing. **In-Young Yeo:** Writing – review & editing, Supervision. **Edward Kim:** Writing – review & editing. **Yann Kerr:** Writing – review & editing. **Thomas Jackson:** Writing – review & editing.

Declaration of Competing Interest

The authors declare that they have no known competing financial interests or personal relationships that could have appeared to influence the work reported in this paper.

Acknowledgment

This work was supported by the Australian Research Council through the Towards P-Band Soil Moisture Sensing from Space Project under Discovery Grant DP170102373, and Linkage, Infrastructure, Equipment and Facility Grants LE0453434 and LE150100047. This work was also supported in part by the China Scholarship Council. The authors wish to thank Pascal Mater and Kiri Mason for their help with the experimental equipment and site maintenance. Thanks also to Mr. Wayne Tymensen for kindly providing the land for the experiment site.

References

Alemohammad, S.H., Jagdhuber, T., Moghaddam, M., Entekhabi, D., 2019. Soil and vegetation scattering contributions in L-band and P-band polarimetric SAR observations. IEEE Trans. Geosci. Remote Sens. 57, 8417–8429.
Basharinov, A.Y., Shutko, A., 1975. Simulation Studies of the SHF Radiation Characteristics of Soils under Moist Conditions.
Chan, S.K., Bindlish, R., O'Neill, P.E., Njoku, E., Jackson, T., Colliander, A., Chen, F., Burgin, M., Dunbar, S., Piepmeier, J., 2016. Assessment of the SMAP passive soil moisture product. IEEE Trans. Geosci. Remote Sens. 54, 4994–5007.
Choudhury, B.J., Schmugge, T.J., Chang, A., Newton, R.W., 1979. Effect of surface roughness on the microwave emission from soils. J. Geophys. Res. Oceans 84, 5699–5706.
Choudhury, B.J., Schmugge, T.J., Mo, T., 1982. A parameterization of effective soil temperature for microwave emission. J. Geophys. Res. Oceans 87, 1301–1304.
Colliander, A., Jackson, T.J., Bindlish, R., Chan, S., Das, N., Kim, S., Cosh, M., Dunbar, R., Dang, L., Pashaian, L., 2017. Validation of SMAP surface soil moisture products with core validation sites. Remote Sens. Environ. 191, 215–231.
Council, N.R., 2010. Spectrum Management for Science in the 21st Century. National Academies Press.
Crow, W.T., Milak, S., Moghaddam, M., Tabatabaeenejad, A., Jaruwatanadilok, S., Yu, X., Shi, Y., Reichle, R.H., Hagimoto, Y., Cuenca, R.H., 2018. Spatial and temporal variability of root-zone soil moisture acquired from hydrologic modeling and AirMOSS P-band radar. IEEE J. Sel. Top. Appl. Earth Obs. Remote. Sens. 11, 4578–4590.
Entekhabi, D., Njoku, E.G., O'Neill, P.E., Kellogg, K.H., Crow, W.T., Edelstein, W.N., Entin, J.K., Goodman, S.D., Jackson, T.J., Johnson, J., Kimball, J., Piepmeier, J.R., Koster, R.D., Martin, N., McDonald, K.C., Moghaddam, M., Moran, S., Reichle, R., Shi, J.C., Spencer, M.W., Thurman, S.W., Tsang, L., Van Zyl, J., 2010. The soil moisture active passive (SMAP) mission. Proc. IEEE 98, 704–716.
Entekhabi, D., Yueh, S., O'Neill, P.E., Kellogg, K.H., Allen, A., Bindlish, R., Brown, M., Chan, S., Colliander, A., Crow, W.T., 2014. SMAP Handbook–Soil Moisture Active Passive: Mapping Soil Moisture and Freeze/Thaw from Space.
Escorihuela, M.J., Chanzy, A., Wigneron, J.P., Kerr, Y.H., 2010. Effective soil moisture sampling depth of L-band radiometry: a case study. Remote Sens. Environ. 114, 995–1001.
Fagerlund, E., Kleman, B., Sellin, L., Svensson, H., 1970. Physical studies of nature by thermal mapping. Earth Sci. Rev. 6, 169–180.
Gao, Y., Colliander, A., Burgin, M.S., Walker, J.P., Chae, C., Dinnat, E., Cosh, M.H., 2017. Multi-frequency radiometer-based soil moisture retrieval algorithm parametrization using in situ validation sites. In: 2017 IEEE International Geoscience and Remote Sensing Symposium (IGARSS). IEEE, pp. 3945–3948.
Gao, Y., Walker, J.P., Ye, N., Panciera, R., Monerris, A., Ryu, D., Rüdiger, C., Jackson, T. J., 2018. Evaluation of the tau–omega model for passive microwave soil moisture retrieval using SMAPEx datasets. IEEE J. Sel. Top. Appl. Earth Obs. Remote. Sens. 11, 888–895.
Garrison, J., Shah, R., Nold, B., Mansell, J., Vega, M., Raymond, J., Bindlish, R., Kurum, M., Piepmeier, J., Kim, S., 2021. SNOOPI: Demonstrating P-band reflectometry from orbit. In: 2021 IEEE International Geoscience and Remote Sensing Symposium (IGARSS). IEEE, pp. 164–167.
Hornbuckle, B., England, A., 2004. Radiometric sensitivity to soil moisture at 1.4 GHz through a corn crop at maximum biomass. Water Resour. Res. 40.
Huang, Y., Liao, G., Li, J., Xu, J., 2018. Narrowband RFI suppression for SAR system via fast implementation of joint sparsity and low-rank property. IEEE Trans. Geosci. Remote Sens. 56, 2748–2761.
ITU, 2015. International Telecommunication Union recommendation: Radio noise. In: ITU-R P.372–12.
Jackson, T.J., 1993. III. Measuring surface soil moisture using passive microwave remote sensing. Hydrol. Process. 7, 139–152.
Jackson, T.J., Schmugge, T.J., 1991. Vegetation effects on the microwave emission of soils. Remote Sens. Environ. 36, 203–212.
Jackson, T.J., Schmugge, T.J., Wang, J.R., 1982. Passive microwave sensing of soil moisture under vegetation canopies. Water Resour. Res. 18, 1137–1142.
Jin, R., Li, Q., Liu, H., 2019. A subspace algorithm to mitigate energy unknown RFI for synthetic aperture interferometric radiometer. IEEE Trans. Geosci. Remote Sens. 58, 227–237.
Johnson, J.T., Jezek, K.C., Aksoy, M., Bringer, A., Yardim, C., Andrews, M., Chen, C.-C., Belgiovane, D., Leuski, V., Durand, M., 2016. The Ultra-wideband Software-Defined Radiometer (UWBRAD) for ice sheet internal temperature sensing: Results from recent observations. In: 2016 IEEE International Geoscience and Remote Sensing Symposium (IGARSS). IEEE, pp. 7085–7087.
Johnson, J.T., Jezek, K.C., Macelloni, G., Brogioni, M., Tsang, L., Dinnat, E.P., Walker, J. P., Ye, N., Misra, S., Piepmeier, J.R., 2021. Microwave radiometry at frequencies from 500 to 1400 MHz: an emerging technology for earth observations. IEEE J. Sel. Top. Appl. Earth Obs. Remote. Sens. 14, 4894–4914.

Kerr, Y.H., Waldteufel, P., Wigneron, J.-P., Delwart, S., Cabot, F., Boutin, J., Escorihuela, M.-J., Font, J., Reul, N., Gruhier, C., Juglea, S.E., Drinkwater, M.R., Hahne, A., Martin-Neira, M., Mecklenburg, S., 2010. The SMOS mission: new tool for monitoring key elements of the global water cycle. Proc. IEEE 98, 666–687.

Kerr, Y.H., Waldteufel, P., Richaume, P., Ferrazzoli, P., Wigneron, J.P., 2019. Algorithm Theoretical Basis Document (ATBD) for the SMOS Level 2 Soil Moisture Processor Development Continuation Project v4.0. SM-ESL (CBSA), p. 150. https://earth.esa.int/eogateway/documents/20142/37627/SMOS-L2-SM-ATBD.pdf:.

Konings, A.G., Piles, M., Rötzer, K., Mccoll, K.A., Chan, S.K., Entekhabi, D., 2016. Vegetation optical depth and scattering albedo retrieval using time series of dual-polarized L-band radiometer observations. Remote Sens. Environ. 172, 178–189.

Konings, A.G., Piles, M., Das, N., Entekhabi, D., 2017. L-band vegetation optical depth and effective scattering albedo estimation from SMAP. Remote Sens. Environ. 198, 460–470.

Koster, R.D., Dirmeyer, P.A., Guo, Z., Bonan, G., Chan, E., Cox, P., Gordon, C., Kanae, S., Kowalczyk, E., Lawrence, D., 2004. Regions of strong coupling between soil moisture and precipitation. Science 305, 1138–1140.

Kraft, D., 1988. A Software Package for Sequential Quadratic Programming.

Lawrence, H., Wigneron, J.P., Demontoux, F., Mialon, A., Kerr, Y.H., 2013. Evaluating the semiempirical H–Q model used to calculate the L-band emissivity of a rough bare soil. IEEE Trans. Geosci. Remote Sens. 51, 4075–4084.

Le Toan, T., Quegan, S., Davidson, M., Balzter, H., Paillou, P., Papathanassiou, K., Plummer, S., Rocca, F., Saatchi, S., Shugart, H., 2011. The BIOMASS mission: mapping global forest biomass to better understand the terrestrial carbon cycle. Remote Sens. Environ. 115, 2850–2860.

Li, X., Al-Yaari, A., Schwank, M., Fan, L., Frappart, F., Swenson, J., Wigneron, J.-P., 2020. Compared performances of SMOS-IC soil moisture and vegetation optical depth retrievals based on tau-omega and two-stream microwave emission models. Remote Sens. Environ. 236, 111502.

Liu, P.-W., De Roo, R.D., England, A.W., Judge, J., 2012. Impact of moisture distribution within the sensing depth on L-and C-band emission in sandy soils. IEEE J. Sel. Top. Appl. Earth Obs. Remote. Sens. 6, 887–899.

Martens, B., Lievens, H., Colliander, A., Jackson, T.J., Verhoest, N.E.C., 2015. Estimating effective roughness parameters of the L-MEB model for soil moisture retrieval using passive microwave observations from SMAPVEX12. IEEE Trans. Geosci. Remote Sens. 53, 4091–4103.

Meguro, A., Shintate, K., Usui, M., Tsujihata, A., 2009. In-orbit deployment characteristics of large deployable antenna reflector onboard engineering test satellite VIII. Acta Astronaut. 65, 1306–1316.

Merlin, O., Walker, J.P., Panciera, R., Young, R., Kalma, J.D., Kim, E.J., 2007. Soil moisture measurement in heterogeneous terrain. In: Modsim International Congress on Modelling & Simulation Land Water & Environmental Management Integrated Systems for Sustainability, pp. 2604–2610.

Mironov, V., Kerr, Y., Wigneron, J.P., Kosolapova, L., Demontoux, F., 2013a. Temperature- and texture-dependent dielectric model for moist soils at 1.4 GHz. IEEE Geosci. Remote Sens. Lett. 10, 419–423.

Mironov, V.L., Bobrov, P.P., Fomin, S.V., 2013b. Multirelaxation generalized refractive mixing dielectric model of moist soils. IEEE Geosci. Remote Sens. Lett. 10, 603–606.

Mo, T., Choudhury, B.J., Schmugge, T.J., Wang, J.R., Jackson, T.J., 1982. A model for microwave emission from vegetation-covered fields. J. Geophys. Res. Oceans 87, 11229–11237.

Newton, R.W., Rouse, J.W., 1980. Microwave radiometer measurements of soil moisture content. IEEE Trans. Antennas Propag. 28, 680–686.

Njoku, E.G., Chan, S.K., 2006. Vegetation and surface roughness effects on AMSR-E land observations. Remote Sens. Environ. 100, 190–199.

Njoku, E.G., Li, L., 1999. Retrieval of land surface parameters using passive microwave measurements at 6-18 GHz. IEEE Trans. Geosci. Remote Sens. 37, 79–93.

Njoku, E.G., Jackson, T.J., Lakshmi, V., Chan, T.K., Nghiem, S.V., 2003. Soil moisture retrieval from AMSR-E. IEEE Trans. Geosci. Remote Sens. 41, 215–229.

Oki, T., Kanae, S., 2006. Global hydrological cycles and world water resources. Science 313, 1068.

O'Neill, P., Bindlish, R., Chan, S., Chaubell, J., Colliander, A., Njoku, E., Jackson, T., 2021a. SMAP Algorithm Theoretical Basis Document (ATBD) Level 2 & 3 Soil Moisture (passive) Data Products Revision G. Jet Propulsion Laboratory, p. 111. https://nsidc.org/data/smap/technical-references:.

O'Neill, P., Chan, S., Bindlish, R., Chaubell, M., Colliander, A., Chen, F., Dunbar, S., Jackson, T., Peng, J., Mousavi, M., Cosh, M., Bongiovanni, T., Walker, J., Wu, X., Berg, A., McNairn, H., Thibeault, M., Martínez-Fernández, J., González-Zamora, Á., Lopez-Baeza, E., Jensen, K., Seyfried, M., Bosch, D., Starks, P., Collins, C.H., Prueger, J., Su, Z., Velde, R.V.D., Asanuma, J., Palecki, M., Small, E., Zreda, M., Calvet, J., Crow, W., Kerr, Y., Yueh, S., Entekhabi, D., 2021b. Calibration and Validation for the L2/3_SM_P Version 8 and L2/3_SM_P_E Version 5 Data Products. Jet Propulsion Laboratory, p. 67. https://nsidc.org/data/smap/technical-references:.

Owe, M., de Jeu, R.A.M., Walker, J., 2001. A methodology for surface soil moisture and vegetation optical depth retrieval using the microwave polarization difference index. IEEE Trans. Geosci. Remote Sens. 39, 1643–1654.

Patton, J., Hornbuckle, B., 2012. Initial validation of SMOS vegetation optical thickness in Iowa. IEEE Geosci. Remote Sens. Lett. 10, 647–651.

Peng, J., Loew, A., Merlin, O., Verhoest, N.E., 2017. A review of spatial downscaling of satellite remotely sensed soil moisture. Rev. Geophys. 55, 341–366.

Prigent, C., Wigneron, J.-P., Rossow, W.B., Pardo-Carrion, J.R., 2000. Frequency and angular variations of land surface microwave emissivities: can we estimate SSM/T and AMSU emissivities from SSM/I emissivities? IEEE Trans. Geosci. Remote Sens. 38, 2373–2386.

Sabaghy, S., Walker, J.P., Renzullo, L.J., Jackson, T.J., 2018. Spatially enhanced passive microwave derived soil moisture: capabilities and opportunities. Remote Sens. Environ. 209, 551–580.

Seneviratne, S.I., Corti, T., Davin, E.L., Hirschi, M., Jaeger, E.B., Lehner, I., Orlowsky, B., Teuling, A.J., 2010. Investigating soil moisture–climate interactions in a changing climate: a review. Earth Sci. Rev. 99, 125–161.

Sharma, J., Prasad, R., Srivastava, P.K., Singh, S.K., Yadav, S.A., Yadav, V.P., 2021. Roughness characterization and disaggregation of coarse resolution SMAP soil moisture using single-channel algorithm. J. Appl. Remote. Sens. 15, 014514.

Shen, X., Walker, J.P., Ye, N., Wu, X., Boopathi, N., Yeo, I.-Y., Zhang, L., Zhu, L., 2021. Soil moisture retrieval depth of P- and L-band radiometry: predictions and observations. IEEE Trans. Geosci. Remote Sens. 59, 6814–6822.

Shen, X., Walker, J.P., Ye, N., Wu, X., Brakhasi, F., Boopathi, N., Zhu, L., Yeo, I.-Y., Kim, E., Kerr, Y., Jackson, T., 2022. Impact of random and periodic surface roughness on P- and L-band radiometry. Remote Sens. Environ. 269, 112825.

Shiklomanov, I.A., 1993. World fresh water resources. In: Gleick, P.H. (Ed.), Water in Crisis: A Guide to the World's Fresh Water Resources. Oxford University Press, New York.

Skou, N., Misra, S., Balling, J.E., Kristensen, S.S., Sobjaerg, S.S., 2009. L-band RFI as experienced during airborne campaigns in preparation for SMOS. IEEE Trans. Geosci. Remote Sens. 48, 1398–1407.

Tabatabaeenejad, A., Burgin, M., Duan, X., Moghaddam, M., 2014. P-band radar retrieval of subsurface soil moisture profile as a second-order polynomial: first AirMOSS results. IEEE Trans. Geosci. Remote Sens. 53, 645–658.

Tabatabaeenejad, A., Chen, R.H., Burgin, M.S., Duan, X., Cuenca, R.H., Cosh, M.H., Scott, R.L., Moghaddam, M., 2020. Assessment and validation of AirMOSS P-band root-zone soil moisture products. IEEE Trans. Geosci. Remote Sens. 58, 6181–6196.

Ulaby, F.T., Moore, R.K., Fung, A.K., 1982. Microwave Remote Sensing Active and Passive-Volume II: Radar Remote Sensing and Surface Scattering and Enission Theory. Artech House Inc.

Ulaby, F.T., Moore, R.K., Fung, A.K., 1986. Microwave Remote Sensing Active and Passive-Volume III: From Theory to Applications. Artech House Inc.

Ulaby, F.T., Long, D.G., Blackwell, W.J., Elachi, C., Fung, A.K., Ruf, C., Sarabandi, K., Zebker, H.A., Van Zyl, J., 2014. Microwave Radar and Radiometric Remote Sensing. University of Michigan Press, Ann Arbor.

Wagner, N., Emmerich, K., Bonitz, F., Kupfer, K., 2011. Experimental investigations on the frequency- and temperature-dependent dielectric material properties of soil. IEEE Trans. Geosci. Remote Sens. 49, 2518–2530.

Walker, V.A., Hornbuckle, B.K., Cosh, M.H., Prueger, J.H., 2019. Seasonal evaluation of SMAP soil moisture in the US corn belt. Remote Sens. 11, 2488.

Wang, J.R., Choudhury, B.J., 1981. Remote sensing of soil moisture content, over bare field at 1.4 GHz frequency. J. Geophys. Res. Oceans 86, 5277–5282.

Wang, J.R., O'Neill, P.E., Jackson, T.J., Engman, E.T., 1983. Multifrequency measurements of the effects of soil moisture, soil texture, and surface roughness. IEEE Trans. Geosci. Remote Sens. 21 (1), 44–51.

Wigneron, J.-P., Chanzy, A., Calvet, J.-C., Bruguier, N., 1995. A simple algorithm to retrieve soil moisture and vegetation biomass using passive microwave measurements over crop fields. Remote Sens. Environ. 51.

Wigneron, J.P., Laguerre, L., Kerr, Y.H., 2001. A simple parameterization of the L-band microwave emission from rough agricultural soils. IEEE Trans. Geosci. Remote Sens. 39, 1697–1707.

Wigneron, J.P., Kerr, Y., Waldteufel, P., Saleh, K., Escorihuela, M.J., Richaume, P., Ferrazzoli, P., Rosnay, P.D., Gurney, R., Calvet, J.C., 2007. L-band microwave emission of the biosphere (L-MEB) model: description and calibration against experimental data sets over crop fields. Remote Sens. Environ. 107, 639–655.

Wigneron, J.P., Jackson, T.J., O'Neill, P., De Lannoy, G., de Rosnay, P., Walker, J.P., Ferrazzoli, P., Mironov, V., Bircher, S., Grant, J.P., Kurum, M., Schwank, M., Munoz-Sabater, J., Das, N., Royer, A., Al-Yaari, A., Al Bitar, A., Fernandez-Moran, R., Lawrence, H., Mialon, A., Parrens, M., Richaume, P., Delwart, S., Kerr, Y., 2017. Modelling the passive microwave signature from land surfaces: a review of recent results and application to the L-band SMOS & SMAP soil moisture retrieval algorithms. Remote Sens. Environ. 192, 238–262.

Yadav, V.P., Prasad, R., Bala, R., Srivastava, P.K., 2020. Synergy of vegetation and soil microwave scattering model for leaf area index retrieval using C-band sentinel-1A satellite data. IEEE Geosci. Remote Sens. Lett. 19, 1–5.

Yardim, C., Johnson, J.T., Jezek, K.C., Andrews, M.J., Durand, M., Duan, Y., Tan, S., Tsang, L., Brogioni, M., Macelloni, G., 2021. Greenland ice sheet subsurface temperature estimation using ultrawideband microwave radiometry. IEEE Trans. Geosci. Remote Sens. 60, 1–12.

Yueh, S., Shah, R., Xu, X., Elder, K., Starr, B., 2020. Experimental demonstration of soil moisture remote sensing using P-band satellite signals of opportunity. IEEE Geosci. Remote Sens. Lett. 17, 207–211.

Zhao, T., Hu, L., Shi, J., Lü, H., Li, S., Fan, D., Wang, P., Geng, D., Kang, C.S., Zhang, Z., 2020. Soil moisture retrievals using L-band radiometry from variable angular ground-based and airborne observations. Remote Sens. Environ. 248, 111958.

Zheng, D., Li, X., Wang, X., Wang, Z., Wen, J., van der Velde, R., Schwank, M., Su, Z., 2019. Sampling depth of L-band radiometer measurements of soil moisture and freeze-thaw dynamics on the Tibetan Plateau. Remote Sens. Environ. 226, 16–25.